Solid Freeform Fabrication 2021: Proceedings of the 32nd Annual International
Solid Freeform Fabrication Symposium – An Additive Manufacturing Conference
Reviewed Paper

The Role of Interface in Additively Manufactured Interpenetrating Composites

J. Allen[1], J. Cheng[1], X. Hu[1], D. A. Splitter[2], M. Gussev[3], A. Shyam[4]

1. Manufacturing Science Division, Oak Ridge National Laboratory, Knoxville, TN 37932
2. Fuels, Engines and Emissions Research Center, Oak Ridge National Laboratory, Knoxville, TN 37932
3. Nuclear Energy and Fuel Cycle Division, Oak Ridge National Laboratory, Oak Ridge, TN 37831
4. Materials Science and Technology Division, Oak Ridge National Laboratory, Oak Ridge, TN 37831

Abstract

Additively Manufactured Interpenetrating Composites (AMIPCs) are a relatively new metal-metal chain composite in development for use in high energy absorption systems. In this system, reinforcing phase of additively manufactured continuous lattice configurations 316L austenitic stainless-steel is in melt infiltrated with a matrix phase of A356 aluminum-silicon casting alloy. Measurements and observations of this material system have shown that weakly bonded or open/porous interface between the reinforcement and matrix phases exhibits dramatically different mechanical properties of AMIPCs, which is not currently well understood. In this work, Finite Element Models (FEM) are used to model the effects of interfaces between the composite phases. Mechanical tensile tests measurements of various composite volume fractions and varying degrees of casting infiltration are also examined and used to show consistency with the FEM results. The outcome provides insight into material design criteria and performance predictions for new hybrid material systems with exceptional damage tolerance.

*This manuscript has been authored by UT-Battelle, LLC, under contract DE-AC05-00OR22725 with the US Department of Energy (DOE).

Introduction

Composite materials have enjoyed a long and successful history in automotive, energy, military and space-based applications owing to the tailorability of material properties such as modulus, strength, thermal conductivity, energy absorption. A fascinating area of composite research centers around metal-matrix composites (MMCs). MMCs have typically been designed by either forming metals with ceramic, glass or carbon fibers (typically refractory materials) in continuous or non-continuous phases with a variety of orientations or by designing an alloy system in such a way as to precipitate out the reinforcing phase *in-situ* during the solidification or heat-treating process [1-2]. One of the barriers for usage of MMC's has traditionally been increased cost of fabrication due to wettability between the reinforcement and matrix material, and complex post machining due to the common presence of ceramics as reinforcement [3].

With the rise of directed energy (laser or electron beam) based additive manufacturing (AM) technologies, recent work has focused on the intelligent design and printing of metallic reinforcing materials with an interpenetrating metallic matrix phase. Moreover, the ability to produce near-net shape complex topologies has reduced the amount of post machining processing of AM produced composites and has enabled a new focus on impact survivability and energy absorption capabilities. Recently, Oak Ridge National Laboratory (ORNL) has developed a metal-metal processing approach for creating metal composites. Termed PrintCast [4-6], this method consists of a two-step processing approach. First, a higher melting temperature metal (e.g., 316L stainless steel) lattice of various volume fractions (though fixed unit cell size) is additively manufactured. The strut size of the lattice determines the volume fraction of the reinforcing and ductile stainless steel in the composite and plays a crucial role in the mechanical response [5], though Pawlowski et al. [6] highlighted that the strut diameters do not need to be homogeneous in size. Second this lattice is infiltrated with molten metal of a lower melting temperature than the lattice (e.g., A356 aluminum alloy) via casting creating a continuous interpenetrating composite of varying geometric constituents.

Preliminary investigations on A356/316L PrintCast composites [4,6] demonstrated in tension testing that these composites are light-weight with low density (<4 g/cm^3), offered good strength up to 400 MPa, and remain ductile with the strains-to-failure larger than 30%. In hypervelocity testing showed PrintCast produced shielding offered energy absorption well beyond those of equivalent mass cladding-based designs [7,8]. The PrintCast approach energy absorption was on-par with the reinforcement material alone while offering in excess of 50% weight savings, showing no signs of spallation on the backside of the composite after hypervelocity impact, making PrintCast an attractive material for applications requiring light-weighting and high specific energy absorption [7]. The PrintCast system has also been shown to have locally tailorable non-linear thermal conductivity properties which offer further optimization potential [9].

Prior work [4-8] on PrintCast composites has not examined the effects that the interface between the reinforcing and matrix phase has on the composite mechanical behavior. However, it has been shown that interfacial bonding is not prominent, and further studies are needed to investigate the critical role that the inter-constituent interface plays in these composites. The present work extends the previous work of 316L AM lattices melt infiltrated with A356 aluminum alloy via centrifugal casting with varying degrees of infiltration. Interfaces are examined via optical microscopy and finite element analysis is used to simulate the deformation and fracture behaviors of the composites. The present results provide insight into the mechanical behavior that can be used in design and optimization of PrintCast composites for future high energy absorption applications.

Experimental Methodology

PrintCast Samples

To create the A356/316L composites by the PrintCast approach, the procedure described in Pawlowski et al [6] was employed. First, lattice preforms, which serve as a reinforcement and define the final shape of the component, were printed using a Renishaw AM250 Selective Laser Melting (SLM) system with gas-atomized 316L powder feedstock (Fe-18Cr-12Ni-2Mo, wt%). The shape of the lattice preform was the same as that described by Pawlowski et al. [6], which was a 40 × 40 × 12 mm lattice encapsulated by a 1 mm skin with an integral sprue for casting infiltration. The lattice configuration was body-centered cubic, with a 2.5 mm unit cell edge-length size. In the second step of PrintCasting, the preforms were infiltrated with molten A356 (Al-7.6Si-0.25Mg-0.2Fe, wt%) aluminum alloy via a spring-driven centrifugal casting machine. The relationship between the lattice strut radius and lattice volume fraction is shown in **Figure 1**.

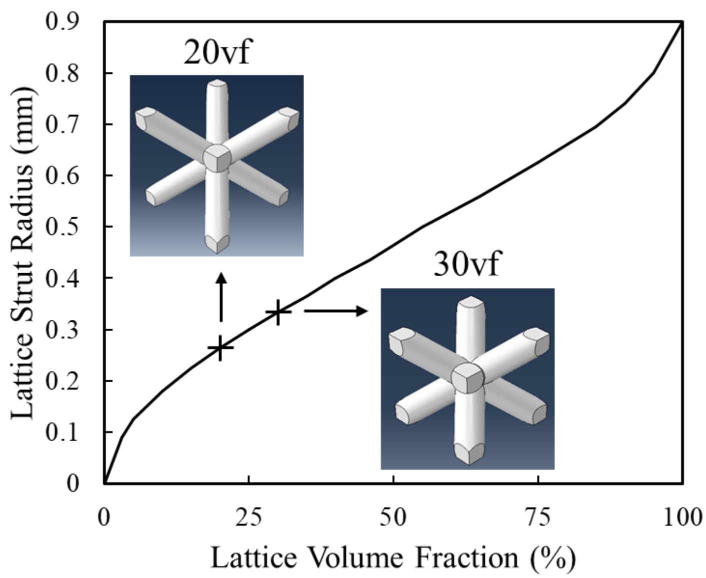

Figure 1: Relationship between bcc lattice strut radius and bcc lattice volume fraction. Based on a unit cell dimension of 2.5 x 2.5 x 2.5 mm.

AM preforms with 20 and 30% volume fraction 316L (all nominal volume fractions) lattices were made by retaining constant the unit cell size while varying the 316L strut diameter. AM preforms with 20% and 30% volume fraction lattices were infiltrated with A356 via centrifugal casting. While the casting process yields a good overall infiltration of the lattices, some areas exhibit poor or even no infiltration due to non-optimized casting procedures. Post infiltration, rectangular cross-section dog bone samples were produced using electric discharge machining to extract blanks for tensile testing with gauge length of 15 mm, 5 mm width (i.e., two unit cells wide), and thickness of 3 mm. Two samples were taken from each infiltrated preform: one sample with good matrix infiltration (i.e., near the sprue entrance of the preform) within the gauge and one that has poor infiltration (i.e., opposite of the sprue entrance, near the bottom of the preform) within the gauge. Images of the samples in the SS-J3 configuration are given in **Figure 2**.

Mechanical Testing

Tensile tests were performed on the samples using a single-column screw driven 2 kN MTS tensile frame, equipped with a 2 kN load cell. Tensile tests were carried out in displacement control mode at 20 °C with a crosshead speed of 0.3 mm per minute, leading to an initial strain rate of $\sim 10^{-3}$ s^{-1}. As previously mentioned, for each 316L volume fraction (20% and 30%), two specimens

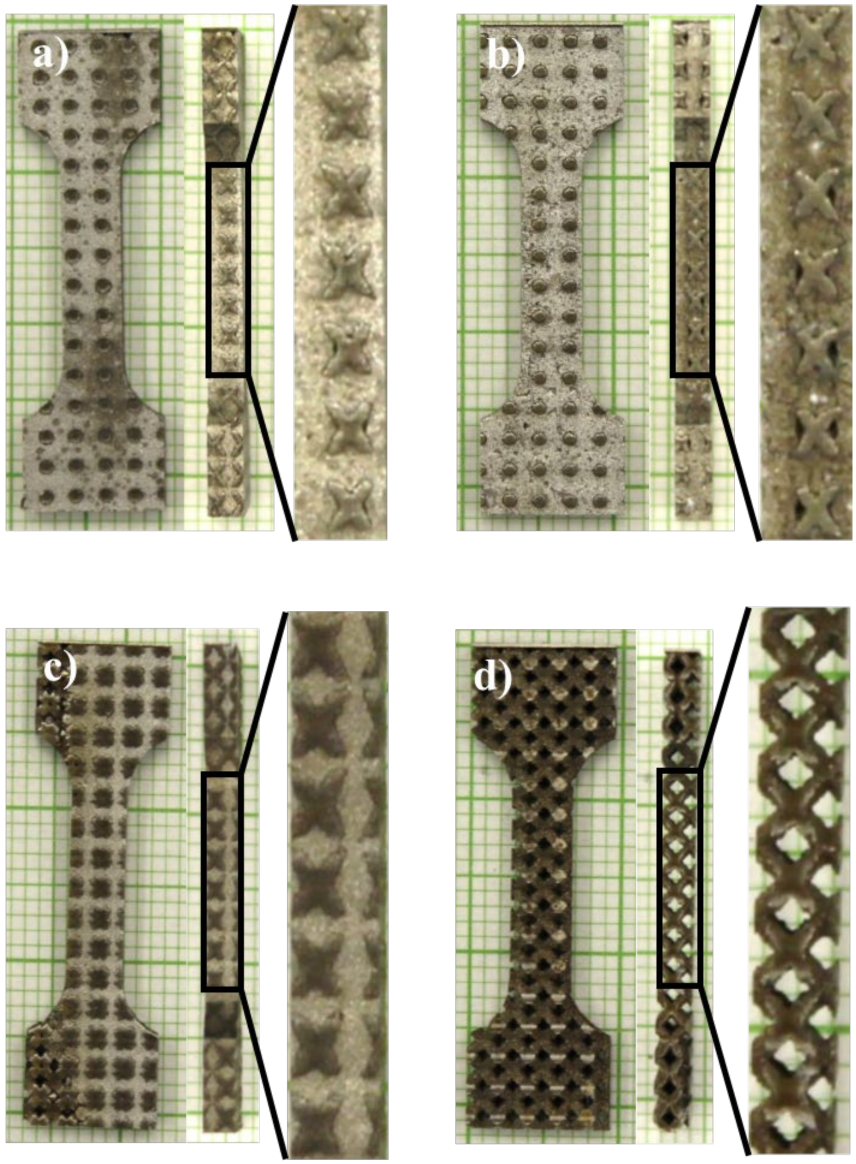

Figure 2: Samples with 20% lattice volume fraction with a) good and b) poor infiltration within the gauge and 30% lattice volume fraction with c) good and d) no infiltration within the gauge.

were tested: one sample with good matrix infiltration and one that has poor infiltration.

Before the tensile testing was performed, the specimens were painted with a random speckle pattern. This surface speckle pattern allows for optical, noncontact strain measurements using a DIC approach [10]. The present work used DIC to measure strains on specimen surface, which is then compared to the FE simulation result. The details can be found in the paper by Cheng, et. al. [8].

A high-resolution Allied Vision GT6600 camera (sensor size: 6576 × 4384 pixels), equipped with a telecentric lens, was mounted on a tripod and used in the experiments reported here. The camera head was precisely positioned in clear focus of the specimen and the lens provided a resolution of around ~5.5 µm per pixel. The Telecentric lenses provided a large depth of focus and was not sensitive to the small shifts of objects towards or away from the camera [10] during tensile loading; this aspect is important for composite materials because they show multiple cracking events during the test. The lens' optic axis was normal to the specimen tensile axis. For each test, one frame per second was recorded and stored for analysis, providing a reasonable compromise between data volume and experiment description. To match the load sensor signal with the DIC image sequence, the time between computers was synchronized. Using the recorded images, the strain fields were calculated using VIC-2D commercial software and a custom application that employed a common 2D DIC algorithm [10].

Optical Microscopy

Differences in infiltration of the 20% volume fraction samples were not clear from the images shown in **Figures 2a** and **2b**. To elucidate these differences, post tensile test 20% volume fraction lattice samples were mounted in two-part epoxy with nickel conductive powder and were ground and polished. A vibromet polisher with 50/50 mix of deionized water and 50 nm diamond suspension was used in the last stage of polishing to ensure a clean surface finish. Samples were imaged optically using a Leica DM 4000 M LED optical microscope at 5x magnification with final images stitched together to provide an entire field of view for each sample. Post tensile test 30% volume fraction lattice samples were not prepared for imaging as one sample showed good matrix infiltration in the gauge length while the other sample showed no infiltration in the gauge length (cf. **Figures 2c** and **2d**).

Finite Element Analysis Methodology

FE analyses were conducted using the commercial FE software ABAQUS/Explicit (2019 version) [11]. The methodology used in this work is the same found in Cheng, et. al. [5]. Two rectangular shape samples consisting of a lattice that was either 20% volume fraction or 30% volume fraction 316L were digitally constructed. For the well infiltrated samples, the 316L lattice and A356 matrix were constructed as two separate objects, as shown in **Figures 3a** and **3b** for the 20% volume fraction case and in **Figures 4a** and **4b** for the 30% volume fraction case. However, for the poorly infiltrated 20% volume fraction sample, modifications were made to the A356 matrix model, which are described in the subsequent section. As for the non-infiltrated 30% volume fraction sample, only the lattice model was used within the FE analysis. Note that the FE model was constructed by matching all surfaces of the gauge section of the 20% volume fraction and 30% volume fraction samples, shown in **Figures 2a-d**. Only the 15 mm × 5 mm × 3 mm size gauge section of the test specimen was considered in the FE model.

The FE model thus assumes no cohesive bonding at the A356/316 L interface, and the two parts interact with each other through a frictional “hard” contact model in ABAQUS [11]. This model assumed no penetration in the normal direction and friction in the shear direction, with a friction coefficient of f = 0.3 that was applied using the penalty friction formulation in ABAQUS. The value of 0.3 was taken from the measured dynamic friction coefficient between Steel and Aluminum [12], where the appendix of Cheng [5] shows the accuracy of this assumption being high with good agreement to physical measurements.

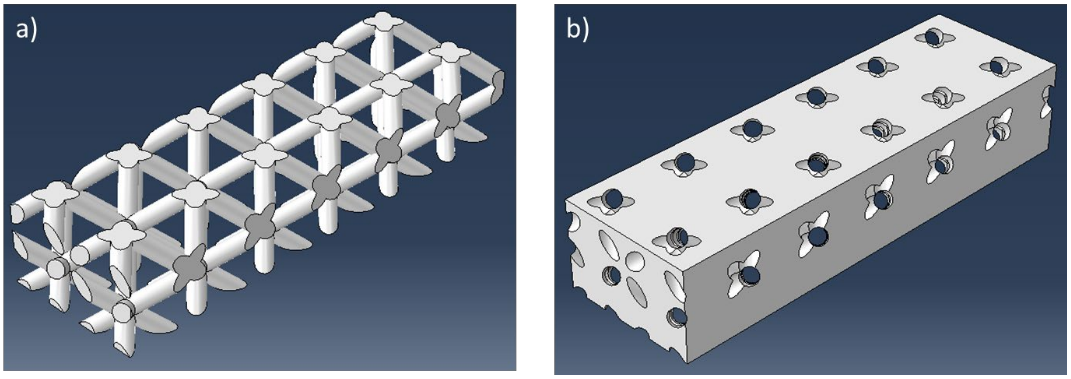

Figure 3: FE model for the a) 356L 20% volume fraction lattice and b) A356 matrix

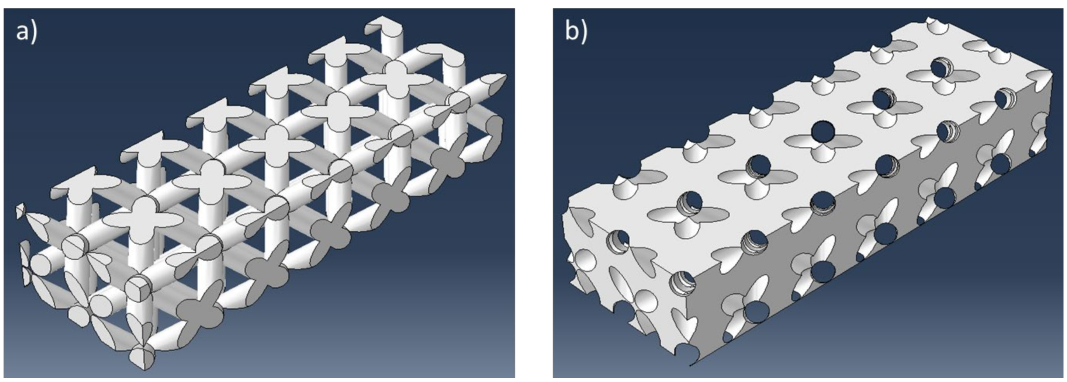

Figure 4: FE model for the a) 356L 30% volume fraction lattice and b) A356 matrix

For each model geometry, four-node linear tetrahedron were used. A quasi-static uniaxial tensile load was applied by defining the nodal velocities on the surfaces of the two ends at 0.0075 mm/s, in opposite directions, to create a constant engineering strain rate of $\dot{\varepsilon}_{\text{applied}} = 1\text{x}10^{-3}$/s, which is comparable to the strain rate of the experimental test. The other surfaces of the models were traction-free, and minimum displacement boundary conditions were applied to eliminate the rigid body translation and rotation. The contact interaction between 316L and A356 surfaces is defined using the general contact module in ABAQUS/Explicit.

The response of 316L and A356 was modeled using a finite deformation isotropic elastic-plastic formulation. Considering the strain rate sensitivity of both 316L and aluminum alloys are low at room temperature [13,14], the model was assumed to be rate independent for simplicity. The density and Young's moduli were obtained from the literature [15] for 316 stainless steel and [16] for A356. The plasticity of each material was defined by tabulating the yield stress as a function of equivalent plastic strain, and the values are plotted in **Figure 5**. The calibration was performed using measurements from monolithic additively manufactured 316 L and monolithic cast A356 uniaxial compression tests [6] as initial values.

For both the A356 and 316L phases, a rate independent damage initiation-propagation model, as described elsewhere [11], was adopted to simulate the failure in the lattice and the matrix. The methodology used is the same as found in Cheng, et. al. [5] except for the damage initiation strain parameters, which were fitted to the experimental stress strain data in the present work. The equivalent plastic strain as a function of stress triaxiality for damage initiation used within this work is shown in **Figure 6**.

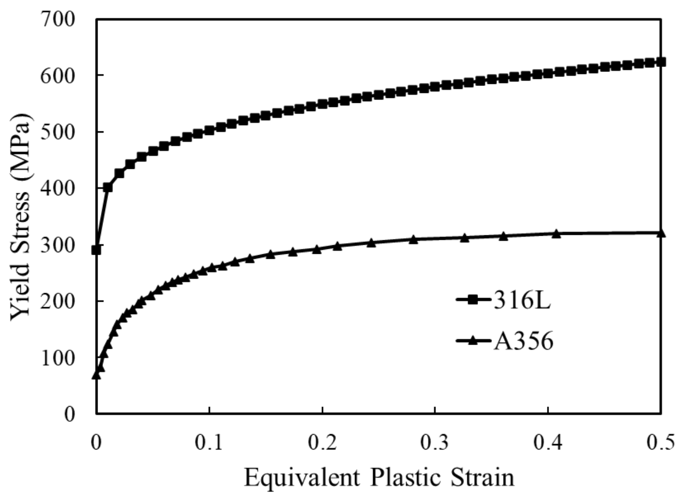

Figure 5: Input yield stress to FE model as a function of equivalent plastic strain.

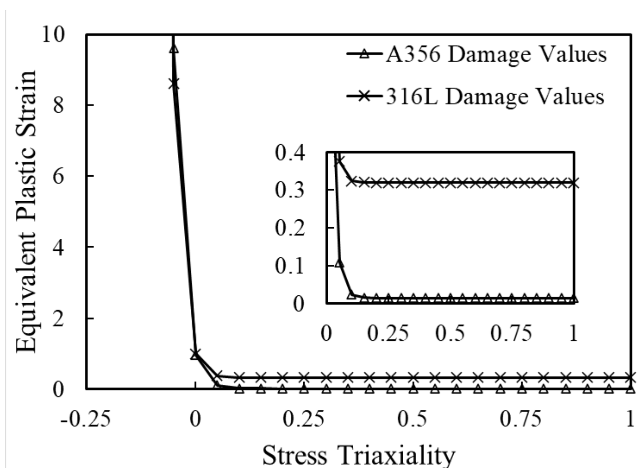

Figure 6: The damage initiation strain (equivalent plastic strain) as a function of stress triaxiality used within the damage initiation model in the present work.

The FE analysis was executed using an explicit time integration algorithm, based on a central difference integration rule at a fixed small time-increment of 10^{-4} s. The semi-automatic mass scaling feature in ABAQUS [11] was used so that each element that had a critical time increment below the target time step size was mass-adjusted to satisfy the Courant-Friedrichs-Lewy (CFL) condition [17] and stabilize the numerical solution. The material property constants used for the modeling, except for the modified damage model parameters discussed above (provided in Table 1 of Cheng, et. al. [5]).

Results and Discussion

The measured stress-strain curves for the 20% volume fraction samples show a large contrast in behavior (**Figure 7a**). The sample taken from near the top of the preform and considered to be well infiltrated shows a peak stress of more than twice that of the sample taken from near the bottom of the preform (considered to be poorly infiltrated). At the same time, the poorly infiltrated sample shows a measured strain to failure of three times that of the sufficiently infiltrated sample. The measured stress-strain curves for the 30% volume fraction samples show similar characteristics as those for the equivalent 20% volume fraction samples, though the sample with the gauge consisting of an open lattice (taken from the bottom of the preform), shows a strain to failure of nearly five times that of the sample considered to be well infiltrated (**Figure 7b**).

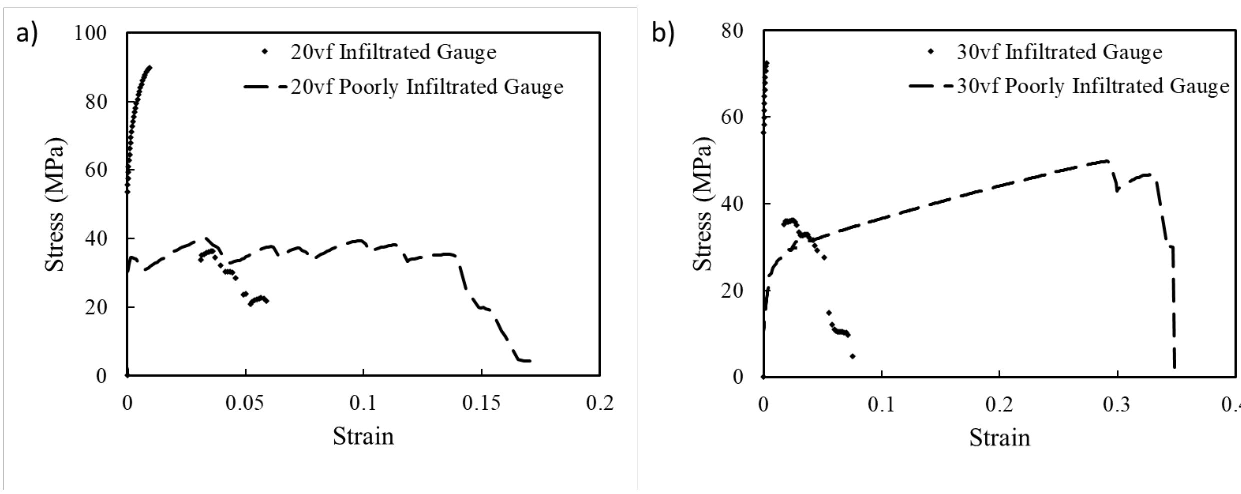

Figure 7: Measured stress-strain curve for a) 20% volume fraction samples with good and poor gauge infiltration and b) 30% volume fraction samples with good and poor gauge infiltration.

While the difference in the quality of gauge infiltration for the 30% volume fraction samples is clear (c.f. **Figures 2c** and **2d**), this is not the case for the 20% volume fraction samples (c.f. **Figures 2a** and **2b**). To better understand this difference, post-tensile samples were cross-sectioned, prepared, and interrogated using optical microscopy. The image in **Figure 8** for the 20% volume fraction taken near the top of the preform shows porosity in two forms: 1) a gap space interface porosity between the 316L lattice and A356 matrix phases and 2) casting or interstitial porosity within the A356 matrix phase. While the matrix phase casting porosity appears as large as 1mm in diameter in some areas, the gap space interface porosity appears on the order of tens of microns in some areas and up to roughly 200 microns in other areas. Within the sample grip, there are areas where poor infiltration is more extensive than the gap space interface and casting porosity alone, but this is assumed to not play a role in the measured stress-strain response; the stress-strain response is attributed to the forces and displacements within the gauge section of the sample only.

The image in **Figure 9** for the 20% volume fraction taken near the bottom of the preform similarly shows gap space interface porosity on the order of tens of microns in some areas and up to 200 microns or larger in others. However, this sample appears to have significant areas of poor infiltration not only within the sample grips, but also within the sample gauge. From two-dimensional cross-sections only, it is impossible to determine the extent of the interfacial and porosity networks, and future work will employ x-ray tomography to better quantify this.

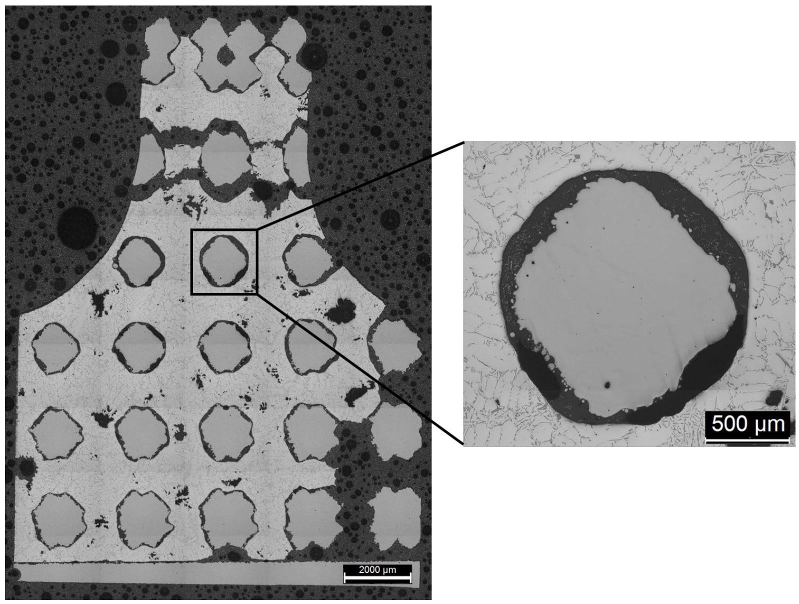

Figure 8: Optical microscope images for the 20% volume fraction sample taken from the top of the preform.

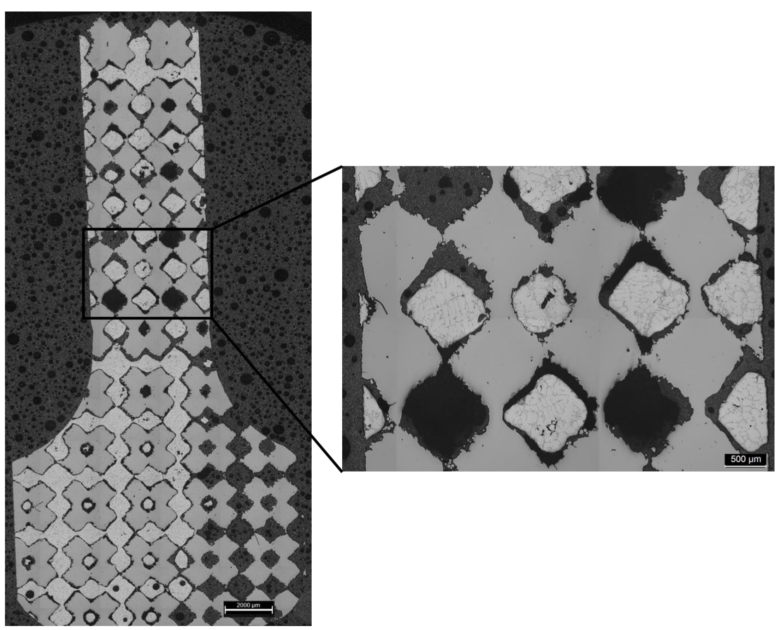

Figure 9: Optical microscope images for the 20% volume fraction sample taken from the bottom of the preform.

To better understand the mechanical behavior of the A356/316L PrintCast composites, prior finite element model geometries were extended to help elucidate the effects of gap space interfaces and porosities. As a baseline, the lattice and matrix geometries shown in **Figures 3a** and **3b**, respectively, were used assuming no gap space interface or porosity using the modeling methodologies outlined earlier and found in Cheng, et. al. [5]. The calculated stress-strain response from this model is show in **Figure 10** along with the experimentally measured stress-strain response. The model results match measurements well with regards to the peak strength and strain to failure and further shows a localized failure behavior as described in previous work [5].

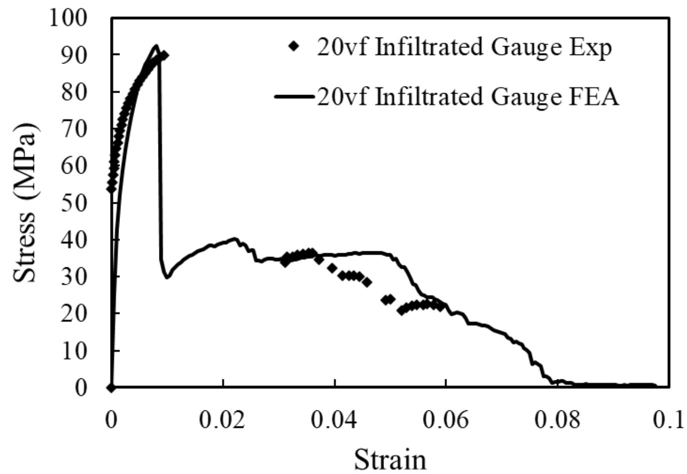

Figure 10: Experimentally measured stress-strain curve and finite element analysis results for 20% volume fraction sample assuming no gap space interface or porosity.

To explore the physical effects of casting porosity, gap space interfacial porosity, and a combination of the two, the matrix material FE model geometry f was modified, such as was shown earlier in poorly infiltrated samples. The casting porosity was introduced as spherical voids with a diameter of 1.5 mm within interstitial spaces between lattices (**Figure 11a**). The gap space interface porosity was introduced by removing a 200 micron wide section of material from the matrix model at the interface between the matrix and lattice (**Figure 11b**). Finally, gap space interface porosity was introduced by again removing a 200 micron wide section of material from the matrix model at the interface between the matrix and lattice along with casting porosity as spherical voids with a diameter of 1.0 mm within interstitial spaces between lattices (**Figure 11c**). In this last case, smaller pores were introduced as material was simultaneously removed from the matrix model leaving smaller interstitial spaces between lattice struts.

The calculated stress-strain curve for each model is shown in **Figures 11d-f** along with the experimentally measured stress-strain curve for the poorly infiltrated sample. From these idealized models, several noticeable trends arise. The addition of an interstitial porosity within the matrix phase yields an appreciable decrease in the initial peak stress, but little to no change in the strain to failure of the composite system (c.f. **Figures 10** and **11d**). Addition of the gap space interfacial porosity results in both an appreciable decrease in the initial peak stress and increase in the strain

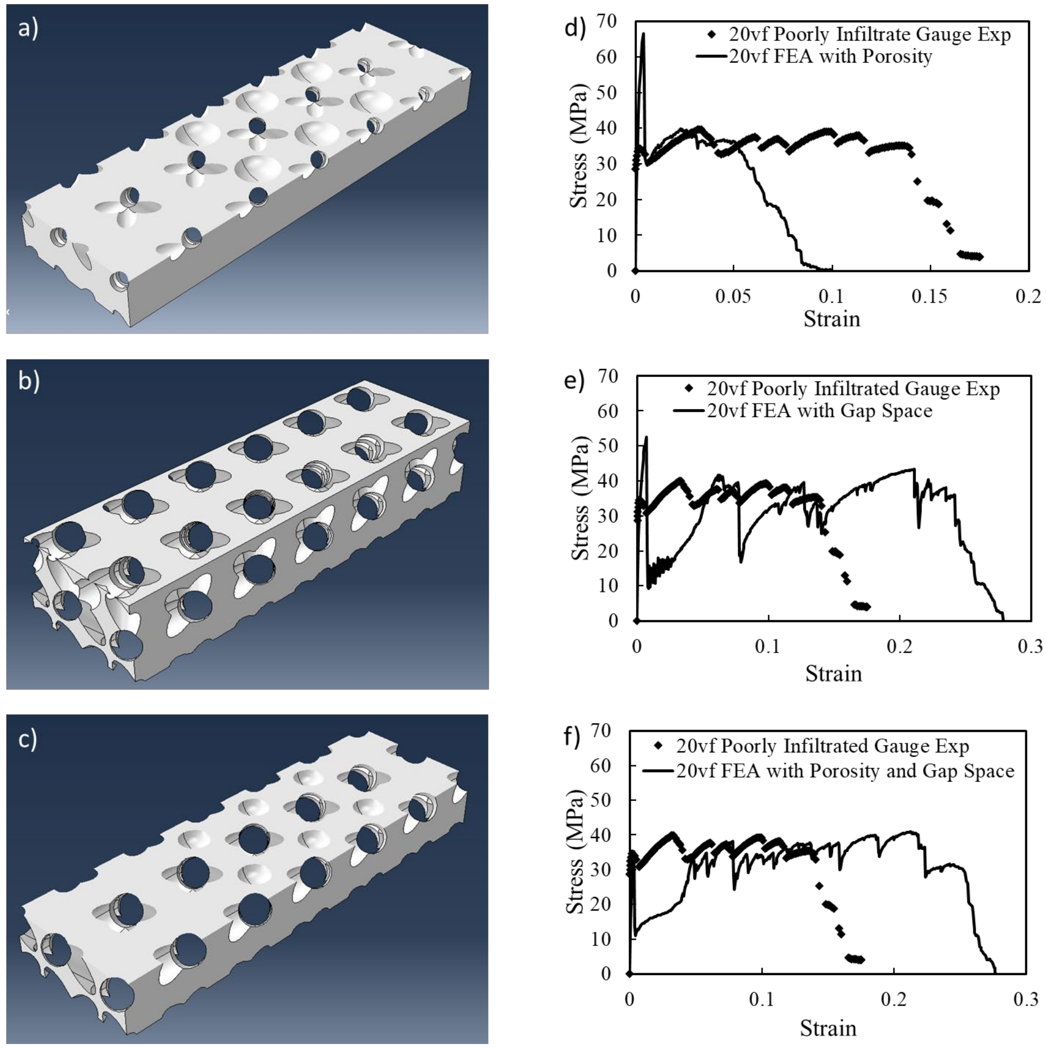

Figure 11: FEA matrix geometry with a) added 1.6 mm diameter spherical porosity (cross section to show pore locations), b) 200 micron wide gap space interface porosity and c) combination of added 1.0 mm diameter spherical porosity and 200 micron wide gap space interface porosity (cross section to show pore locations), along with respective calculated stress-strain results d)-f).

to failure of the composite system transitioning to a delocalized failure type behavior (c.f. **Figures 10** and **11e**) while further addition of porosity to this model yields additional decrease in the initial peak stress but no further change in the strain to failure behavior (c.f. **Figures 10** and **11f**). The model that accounts for both gap space interfacial porosity and interstitial porosity yields a peak stress that matches well with experimentally measured data. However, both models that include gap space interfacial porosity overpredicted strain to failure by ~50%. As can be seen in **Figures 8** and **9**, the 200 micron gap space used tends towards the upper limit as seen in optical images and is constant throughout the models, not taking into account the variability in the actual gap space thickness.

To model the 30% volume fraction sample with good infiltration, the lattice and matrix geometries shown in **Figures 4a** and **4b**, respectively, were used, and again assumed no gap space interface or interstitial porosity. The calculated stress-strain response from this model is show in **Figure 12** along with the experimentally measured stress-strain response. While the model matches the measured strain to failure and the localized failure behavior well , the calculated peak strength is overpredicted by ~25%. The 30% volume fraction sample with poor infiltration was modeled using only the lattice model (open lattice) shown in **Figure 4a** and the calculated stress-strain response is given in **Figure 13** along with the experimentally measured stress-strain response. Again, the model matches well with respect to strain to failure and captures the delocalized failure behavior but again over predicts the stress by ~25%.

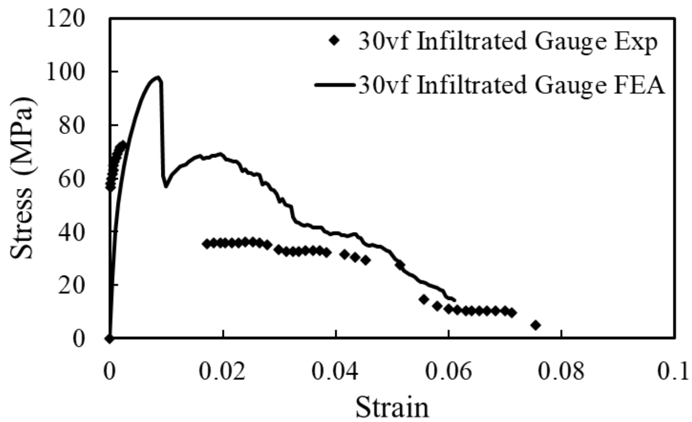

Figure 12: Experimentally measured stress-strain curve and finite element analysis results for 30% volume fraction sample assuming no gap space interface or porosity.

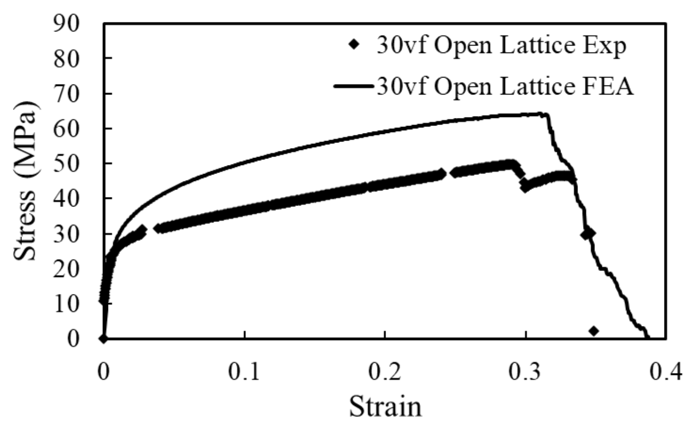

Figure 13: Experimentally measured stress-strain curve and finite element analysis results for 30% volume fraction sample assuming lattice only (open lattice behavior).

Previous work by Cheng et. al. [5] discussed the mechanisms that contribute to failure within the A356/316L PrintCast composite system, especially with regard to localized and delocalized failure behavior. However, that work focused on composite systems with no assumed gap space interface or interstitial porosity. While the same mechanisms may help explain the behaviors described within this work, further analysis is needed. Regardless, the importance of the different interfaces within PrintCast composites and their effects on the mechanical behavior cannot be understated. While FEA predicts that interstitial porosity appears to have minor effects on the overall composite behavior, gap space interface porosity appears to influence much larger changes that may increase overall energy absorption capability. To increase the accuracy of model predictability, future modeling efforts should be recalibrated to take into consideration interfacial porosity effects, most notably the gap space between the lattice and matrix phases.

Summary

In this work, the mechanical behavior of a 316L/A356 PrintCast composite was investigated with consideration of two types of interfaces: porosity (gap space interface) between the reinforcing and matrix phase and porosity within the matrix due to poor infiltration. Optical microscopy showed that gap space interface porosity can range from the tens of microns to hundreds of microns while porosity due to poor infiltration can be as large as 1 mm or more with complete lack of infiltration yielding an open lattice structure.

Mechanical testing showed that PrintCast samples with good matrix infiltration had high initial strength but much lower strain to failure (localized failure) than samples with poor or no matrix infiltration. The mechanical behavior of poorly infiltrated samples showed delocalized failure behavior with lower initial strength and large strain to failure approaching that of an open lattice in the limit of a complete lack of infiltration.

Finite Element Analysis was used to help elucidate the effects that the different interfaces have on the mechanical response of PrintCast composites. Initial models were developed with no gap space and complete matrix infiltration and calibrated to the mechanical response of samples showing good matrix infiltration. Refined models included gap space interface porosity between the reinforcement and matrix phases, large porosity within the matrix phase to model poor infiltration and a combination of both types of interfaces. The models indicated that porosity played a role in reduction of the initial strength of the matrix material but had little to no effect in the strain to failure behavior. Gap space interface porosity showed greater reduction of the initial strength of the matrix material and large increases in the strain to failure behavior. The model with a combination of gap space interface porosity and matrix porosity showed further decrease in the initial strength of the matrix material but yielded no additional strain to failure.

This work highlights the importance of the different interfaces within PrintCast composites and their effects on the mechanical behavior. To increase the accuracy of model predictability, future modeling efforts should be recalibrated to take into consideration interfacial porosity effects, most notably the gap space between the lattice and matrix phases. Because of the large increases in strain to failure, future work should also focus on the effects of the gap space on the energy absorption capabilities of PrintCast composites.

Acknowledgements

This research was sponsored by the US Department of Energy, Office of Vehicle Technology, under a prime contract with Oak Ridge National Laboratory (ORNL). ORNL is managed by UT-Battelle, LLC for the U.S. Department of Energy under Contract DE-AC0500OR22725. This work was funded by the DOE Office of Energy Efficiency & Renewable Energy and Vehicle Technologies Office under the Powertrain Materials Core Program managed by Jerry Gibbs.

References

1. Chawla, K.K., *Metal Matrix Composites.* Materials Science and Technology, 2006: p. 62.
2. Miracle, D.B., *Metal matrix composites - From science to technological significance.* Composites Science and Technology, 2005. **65**(15-16): p. 2526-2540.
3. Ibrahim, I.A., F.A. Mohamed, and E.J. Lavernia, *Particulate reinforced metal matrix composites — a review.* Journal of Materials Science, 1991. **26**(5): p. 1137-1156.
4. Pawlowski, A.E., Splitter, D.A., Muth, T.R., Shyam, A., Carver, K., Dinwiddie, R.B., Elliott, A.M., Cordero, Z. and French, M., *Producing Hybrid Metal Composites by Combining Additive Manufacturing and Casting.* Advanced Materials & Processes, 2017. **175**(7): p. 16-21.
5. Cheng, J., Gussev, M., Allen, J., Hu, X., Moustafa, A.R., Splitter, D.A. and Shyam, A., D*eformation and failure of PrintCast A356/316 L composites: Digital image correlation and finite element modeling*. Materials & Design, 2020. **195**: p.109061.
6. Pawlowski, A.E., Cordero, Z.C., French, M.R., Muth, T.R., Carver, J.K., Dinwiddie, R.B., Elliott, A.M., Shyam, A. and Splitter, D.A., *Damage-tolerant metallic composites via melt infiltration of additively manufactured preforms.* Materials & Design, 2017. **127**: p. 346-351.
7. French, M., Yarberry, W., Pawlowski, A.E., Shyam, A., Splitter, D.A., Elliott, A.M., Carver, K. and Cordero, Z., *Hypervelocity Impact of Additively Manufactured A356/316L Interpenetrating Phase Composites*, 28th Annual International Solid Freeform Fabrication Symposium, 2017.
8. Poole, L.L., Gonzales, M., French, M.R., Yarberry III, W.A., Moustafa, A.R. and Cordero, Z.C., *Hypervelocity impact of PrintCast 316L/A356 composites.* International Journal of Impact Engineering, 2020. **136**: p.103407.
9. Moustafa, A.R., Dinwiddie, R.B., Pawlowski, A.E., Splitter, D.A., Shyam, A. and Cordero, Z.C., *Mesostructure and porosity effects on the thermal conductivity of additively manufactured interpenetrating phase composites.* Additive Manufacturing, 2018. **22**: p. 223-229.
10. H. Schreier, J.J. Orteu, M.A. Sutton, Image Correlation for Shape, Motion and Deformation Measurements: Basic Concepts, Theory and Applications, 2009.
11. Simulia, Abaqus / CAE 6.14 User''s Manual, Dassault Systémes Inc, Provid. RI, USA, 2014 1–1146.
12. Santos, A. , Córdoba, E., Ramirez, Z., Sierra, C., Ortega, Y., *Determination of the coefficient of dynamic friction between coatings of alumina and metallic materials*, Journal of Physics: Conference Series, 2017. **931**(1), p. 012042.
13. Li, Z., Voisin, T., McKeown, J.T., Ye, J., Braun, T., Kamath, C., King, W.E. and Wang, Y.M., *Tensile properties, strain rate sensitivity, and activation volume of additively manufactured 316L stainless steels*, International Journal of Plasticit, 2019. **120**: p. 395-410.

14. Yan, S.L., Yang, H., Li, H.W. and Yao, X., *Variation of strain rate sensitivity of an aluminum alloy in a wide strain rate range: Mechanism analysis and modeling*, Journal of Alloys and Compounds, 2016. **688**: p.776-786.
15. Wang, Y.M., Voisin, T., McKeown, J.T., Ye, J., Calta, N.P., Li, Z., Zeng, Z., Zhang, Y., Chen, W., Roehling, T.T. and Ott, R.T., *Additively manufactured hierarchical stainless steels with high strength and ductility.* Nature materials, 2018. **17**(1): p. 63-71.
16. Gupta, S., Abotula, S. and Shukla, A., *Determination of johnson–cook parameters for cast aluminum alloys.* Journal of engineering materials and technology, 2014. 136(3).
17. T. Belytschko, in: Thomas J.R. Hughes (Ed.), The Finite Element Method: Linear Static and Dynamic Finite Element Analysis, 4, Comput. Civ. Infrastruct. Eng. 2008, pp. 245–246.